GSA Data Repository 2015311

Supplementary information - South Atlantic Opening: a plume induced breakup?

T. Fromm[1] *, L. Planert, W. Jokat, J. H. Behrmann, T. Ryberg and M. Weber*

Here we provide a short description of the methods used and present error statistics for the velocity models (Table DR1–Table DR4), data examples of recorded seismic sections (Fig. DR1), picked and traced travel times as well as the corresponding ray paths (Fig. DR2–Fig. DR5). Resolution (Fig. DR6, Fig. DR7) and DWS (derivated weight sum, Fig. DR10–Fig. DR11) plots demonstrate the model uncertainty. The different types of plots are due to different modelling approaches described in the methods section.

1.1 Methods

Data acquisition and processing The marine seismic source consisted of a $8 \times 8\,l$ G-gun array ($64\,l$ or 3905 cu. in. in total) operated at 200 bar (2900 psi) in 8 m water depth. Profiles 100 and 150 were shot with an interval of 90 s resulting in approx. 230 m shot distance and 13 km separation between the OBH (Ocean Bottom Hydrophone), while profiles 2 and 3 had a denser shot and receiver distribution (60 s shooting interval, 125 m shot distance and 7.6 km OBH separation). The dynamite shots onshore were loaded with charges of 250 to 400 kg with approx. 22–52 km separation. The distance between the land receivers was approx. 6 km. The number of OBH, land receivers and dynamite shots varied between the profiles. Profile 100 (720 km long) extends along the ridge axis and consists of 27 OBH, 48 land receivers and 8 dynamite shots. Profile 150 (480 km long) crosses Walvis Ridge 600 km offshore and consists of 27 stations. Profile 3 (600 km long) crosses Walvis Ridge 200 km offshore and consists of 74 stations. And finally profile 2 (670 km long) crosses the Angola Basin and the landfall of Walvis Ridge. It consists of 39 OBH, 52 landstations and 7 dynamite shots. Data examples for all profiles are shown in Fig. DR2–Fig. DR5. The data was processed using a standard procedure including relocation of OBH and projection on straight lines. Travel times were picked on the processed seismic section after applying a deconvolution and time and offset variant bandpass filtering.

Modelling and uncertainties We followed a top to bottom approach, first fitting the upper layers before modelling the lower ones. The upper sedimentary strata and basement topography was constrained by single channel streamer records of the airgun shots (Fig. DR1). Arrival times from the reflection seismic data were converted to depth using the velocity information from the OBS. This starting model was then further refined using two different methods.

[1]Tanja.Fromm@awi.de

For profiles 100 and 150 we used a layer based method (the rayinvr software package, Zelt and Smith, 1992) and for profiles 2 and 3 a tomographic approach (tomo2D software package, Korenaga et al., 2000). In the layer based method the model is represented by separate layers with velocity nodes distributed with variable spacings along the upper and lower boundaries. The velocity field between the nodes is linearly interpolated and boundaries can be reflective but might also only be used to change the velocity gradient. The layer boundaries do not necessarily reflect geological boundaries. The fit between the modelled and theoretical arrivals is shown in Fig. DR8 and Fig. DR9 along with the corresponding ray paths.

The velocity structure for the tomographic models is defined on a dense irregular grid of velocity nodes. We used a horizontal node spacing of 250 m and 500 m in the marine part and 1 km in the less-well resolved land part of the models. Vertical node spacing increases linearly from 100 m at the seafloor to 250 m at depths equal and greater than 40 km below seafloor. Model regularization in the inversion is accomplished by the use of correlation lengths, which control the size of those model areas affected by a velocity update of a grid cell. We used a horizontal correlation length of 1.5 km at the seafloor, which linearly increases to 10 km at the model bottom, and a vertical correlation length with corresponding values of 0.3 km and 2 km, respectively. Reflectors are implemented as floating reflectors, which are independent from the underlying velocity grid. For the reflector nodes, the appropriate regularization length scales are taken from the horizontal 2D velocity correlation lengths at the corresponding depths.

For the modelling of the crustal portions we utilized spatially variable velocity damping for the overlying sedimentary portions and incorporated velocity jumps into the input models at primary features such as the basement and the crust-mantle boundary (Moho).

The resolution for the forward model is derived from the diagonal elements of the resolution matrix. They indicate the linear dependence of the true model and the relative number of rays sampling each model parameter. Values greater than 0.5 are considered reasonably well resolved within the given uncertainty (Lutter et al., 1990), here $\Delta v = \pm 0.2$ km/s, $\Delta d = \pm 2$km. The resolution of the velocity nodes for the forward models is shown in Fig. DR6 and Fig. DR7.

For the tomographic modelling the resolution can be estimated from the derivative weight sum (DWS). The DWS is the column-sum vector of the normalized derivative matrix and represents a weighted sum of the ray path length influenced by a model parameter and, due to the matrix normalization, it also depends on the pick-uncertainty of each ray. Altogether, this results in a rough assessment of solution sensibility on the basis of data quantity and quality. Hence, a high DWS value can be ascribed either to a denser sampling of rays or to an accumulation of higher quality rays with smaller pick-uncertainties. The DWS values for the tomographic models is shown in Fig. DR10 and Fig. DR11.

The uncertainties for the travel time picks were manually assigned varying between 60 ms and 250 ms. The largest uncertainties were assigned to the land stations, where the signal to noise ratio was partly poor, especially for the PmP phases. Altogether 188.949 picks were traced and all models reached consistency with the picked arrivals within an RMS deviation of 118 ms or less. More details on the modelling errors are listed in Table DR1–Table DR4. The model uncertainty was estimated by changing velocities and depth nodes until the resulting travel time residuals became larger than the pick uncertainties (for profile 100 and 150). This results in $\Delta v = \pm 0.2$ km/s and $\Delta d = \pm 2$ km for reflector depths.

Profile i ntersections There are two intersections between the presented profiles. Profiles 100 and 2 intersect onshore at km 466 and 410, respectively. Profile 100 and 3 intersect offshore at km 235 and 222. For example, Fig. DR12 presents a comparison of the velocity depth relation at the intersection of profiles 100 and 2. The forward modelled P100 shows a linear velocity depth relation with discrete steps in velocity at the layer boundaries. In contrast, the tomography of P2 has a smooth velocity depth relation without discrete steps. The velocity increase at the crust mantle boundary is accommodated over a depth range and not coupled to the Moho reflection.

The velocity depth relations are generally in good agreement, although P100 reveals slightly higher velocities in the lower crust (6.9 km/s instead of 6.6 km/s at 30 km depth) and lower velocities at 35 km depth (7.2 km/s instead of 7.6 km/s). This discrepancy can be explained with the different modelling approaches. The layer based velocity model has significantly less parameter and therefore averages velocities. The velocity of 7.2 km/s at the Moho of P100 fits well with the average 7.1 km/s of the strong gradient from 6.6 to 7.6 km/s between 30 and 35 km depth of P2, which represents the Moho in the tomographic approach. The difference in Moho depth is related to the different velocities in the lower crust. Seismic modelling solves a non-linear problem and the reflector depth depends on the velocities. Higher velocities inevitable lead to greater reflector depths.

Additionally, the geometry of the profile layout has a large effect on the revealed geological structures. Especially in such a highly variable environment as the Walvis Ridge with its seamounts and local intrusions. The geometry of the profile layout has a strong influence on the visibility of the small scale local intrusions.

Unit	**n**	t_{rms}/s	χ^2
Sediments (incl. refl.)	1945	0.061	0.753
Crust (airgun shots)	7133	0.097	0.615
Crust (dynamite shots)	198	0.222	1.427
Mantle	396	0.311	2.128
Boundary			
Moho (airgun shots)	755	0.203	1.022
Moho (dynamite shots)	47	0.374	2.290
Basement	141	0.084	1.464
Total	10550	0.115	0.726

Table DR1: Summarized error statistics for model P100 showing the number of traveltime picks (n), the RMS error (t_{rms}) and the normalized χ^2 value for different model units and corresponding boundaries. Results for the model units combine refractions (respec-tive turning rays); results for the boundaries combine respective reflections. Note that the result for 'Sediments' includes some additional intra-sedimentary reflections. The basement is further constrained by single-channel streamer data. Note that the uncer-tainty for the sparse land data is usually larger than for the marine data.

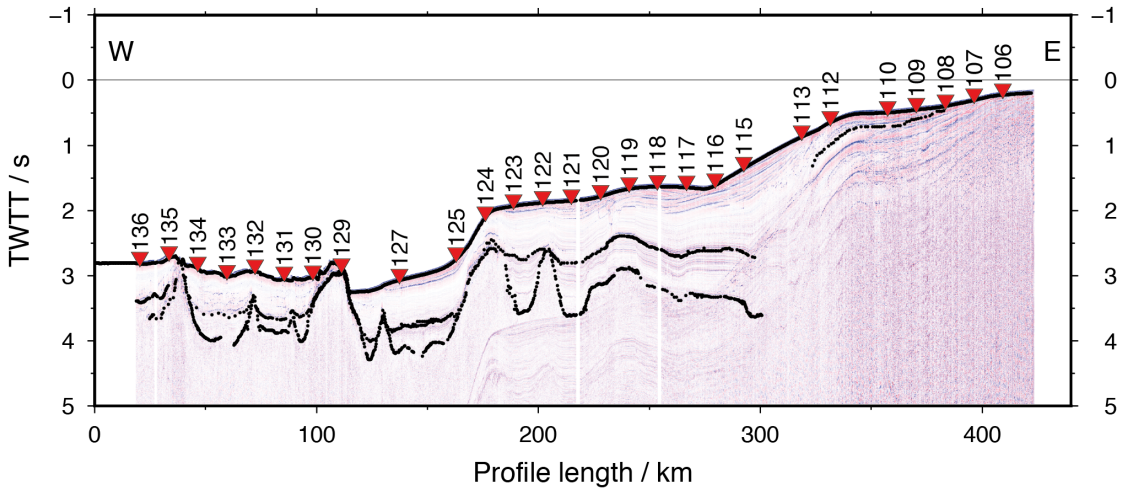

Fig. DR1: Single channel reflection data for P100. Sediments and basement reflections (black dots) have been incorporated into the starting model.

Unit	**n**	t_{rms}/s	χ^2
Sediments	942	0.070	0.855
Crust	5729	0.074	0.475
Mantle	244	0.094	0.494
Boundary			
Moho	2369	0.097	0.558
Basement	517	0.101	1.803
LVZ (top)	65	0.045	0.208
LVZ (bottom)	254	0.092	0.921
Total	10120	0.082	0.607

Table DR2: Summarized error statistics for model P150 (c.f. caption of Table DR1). The low velocity zone (LVZ) north of the ridge is bound by reflections from the top and bottom but remains relatively poor resolved due to missing refracted phases (see Fig. DR7).

Unit	**n**	t_{rms}/s	χ^2
Sediment (incl. Refl.)	8223	0.030	0.77
Crust (airgun shots)	20784	0.053	1.09
Crust (dynamite shots)	239	0.102	2.87
Mantle (airgun shots)	16911	0.087	2.12
Mantle (dynamite shots)	34	0.079	1.72
Boundary			
Basement	1175	0.063	1.11
Intra-crustal	2156	0.063	1.12
Moho (airgun shots)	8536	0.056	0.97
Moho (dynamite shots)	123	0.075	1.56
Total	58181	0.061	1.34

Table DR3: Summarized error statistics for model P2 (c.f. caption of Table DR1). Note that the uncertainty for the sparse land data is usually larger than for the marine data.

Unit	**n**	t_{rms}/s	χ^2
Sediment (incl. Refl.)	6542	0.029	1.06
Flows	10869	0.049	1.3
Crust	54989	0.054	1.82
Mantle	15483	0.082	1.88
Boundary			
Basement	3090	0.023	0.62
Intra-crustal 1	3867	0.034	0.72
Intra-crustal 2	8719	0.090	5.01
Moho (Angola Basin)	1437	0.075	3.51
Moho (WR and Walvis Basin)	5094	0.097	4.97
Total	110090	0.059	2.08

Table DR4: Summarized error statistics for model P3. The 'Flows' unit represents the uppermost crustal layer beneath Walvis Ridge and further south in the Walvis Basin. 'Intra-crustal 1' is the base of the 'Flows' unit; 'Intra-crustal 2' combines top HVLCB and top underplating.

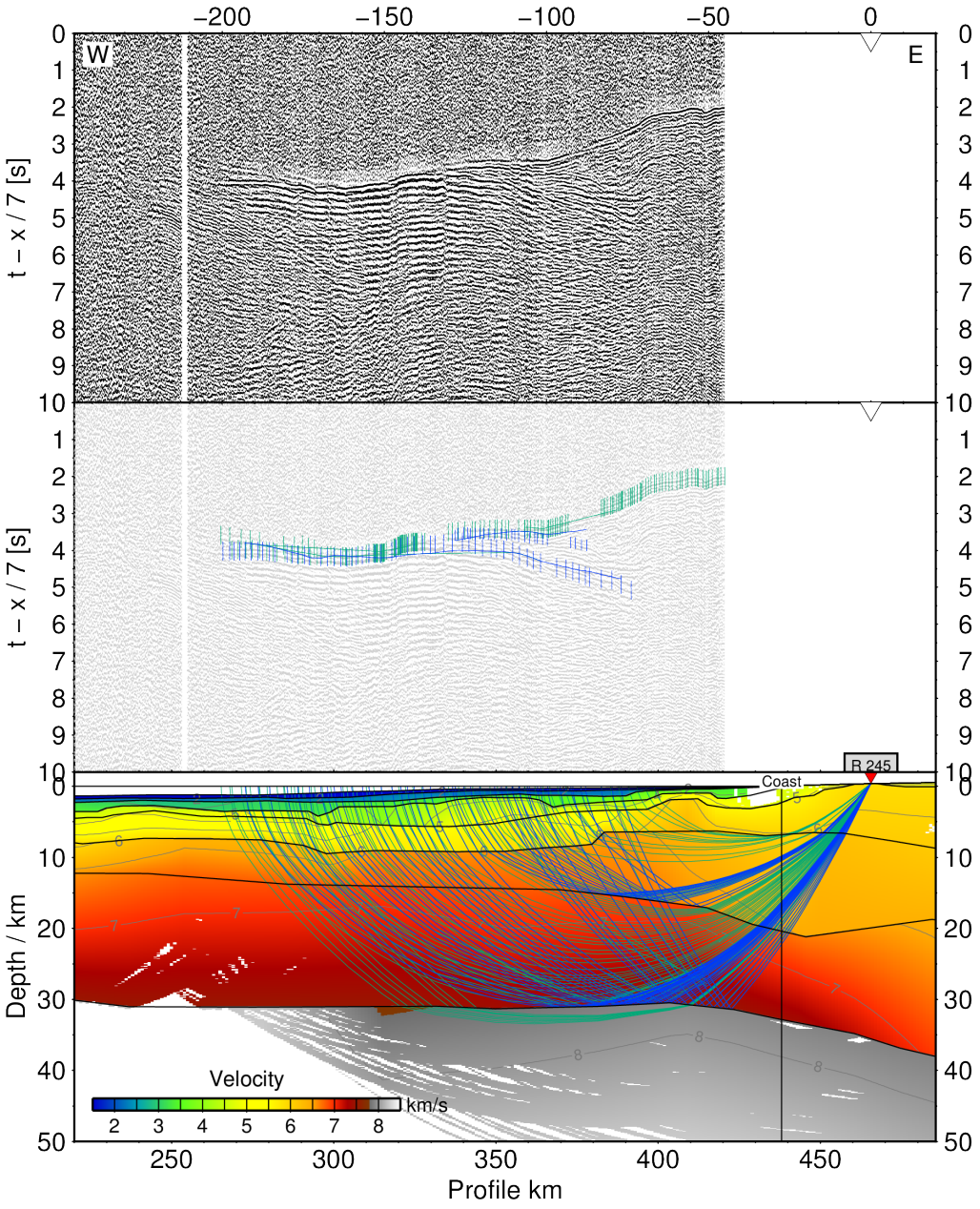

Fig. DR2: Data example for P100 showing recorded seismic data (top), traced arrivals (center) and ray coverage (bottom). The data are bandpass filtered with 3.5-13 Hz corner frequencies and amplified with an automated gain control (AGC) of 1 s. Picks are vertical bars with variable length representing the pick uncertainty. The number of drawn rays is reduced for clarity. This section shows airgun shots recorded by a receiver onshore. The data quality is excellent with long offsets and clear PmP and Pn phases.

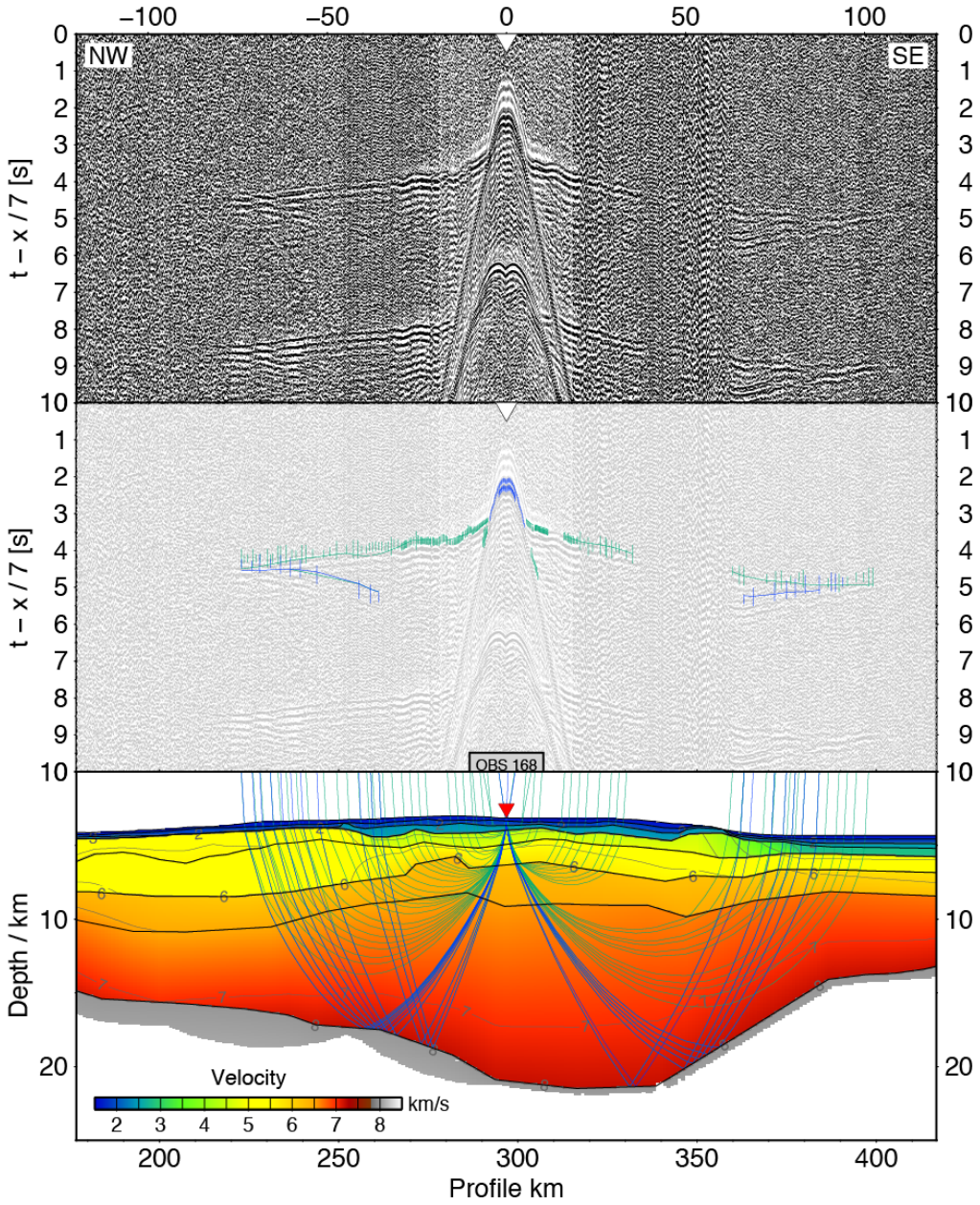

Fig. DR3: Data example for P150 with the same plotting parameter as used for Fig. DR2. This station shows clear crustal arrivals and Moho reflection.

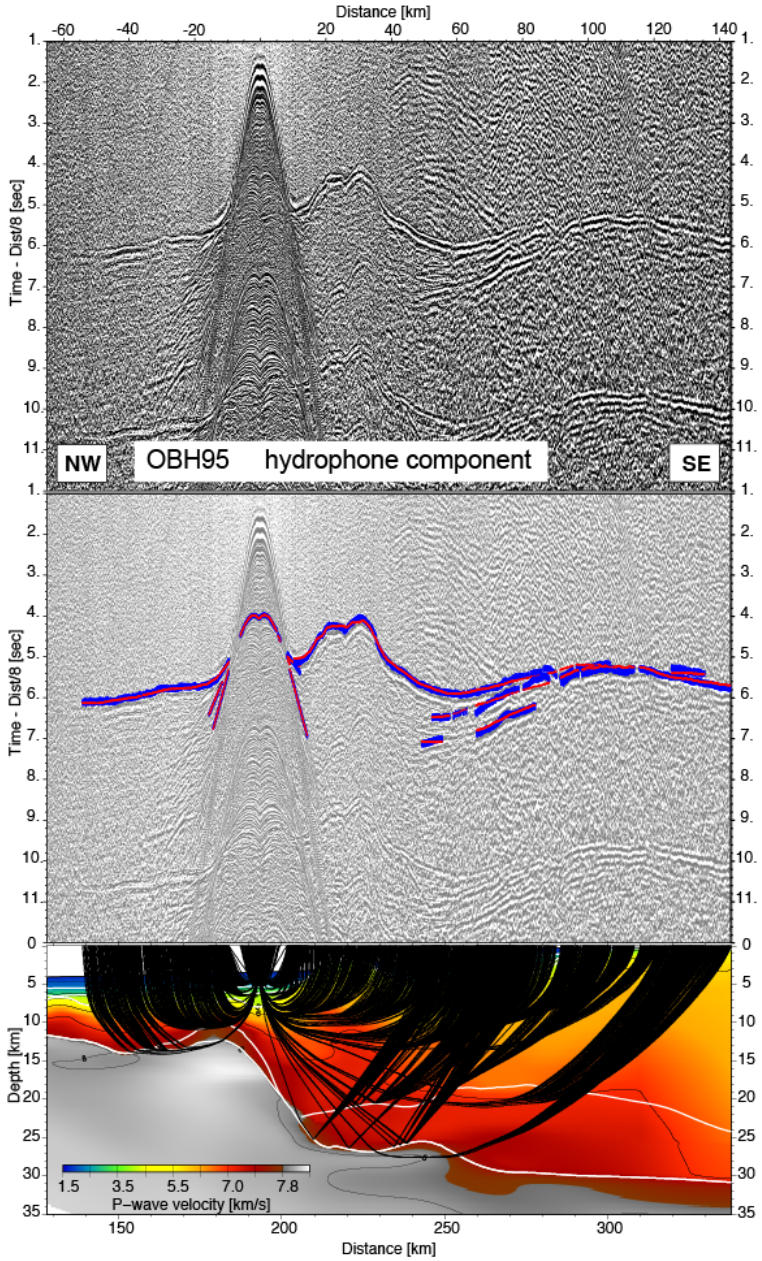

Fig. DR4: (Top): Seismic record section (reduced to 8 km/s) of OBH95 on profile 2. (Center): Computed traveltimes (red dots) and associated pick-uncertainties (blue bars). (Bottom): Corresponding ray paths through the final tomographic solution of profile 2.

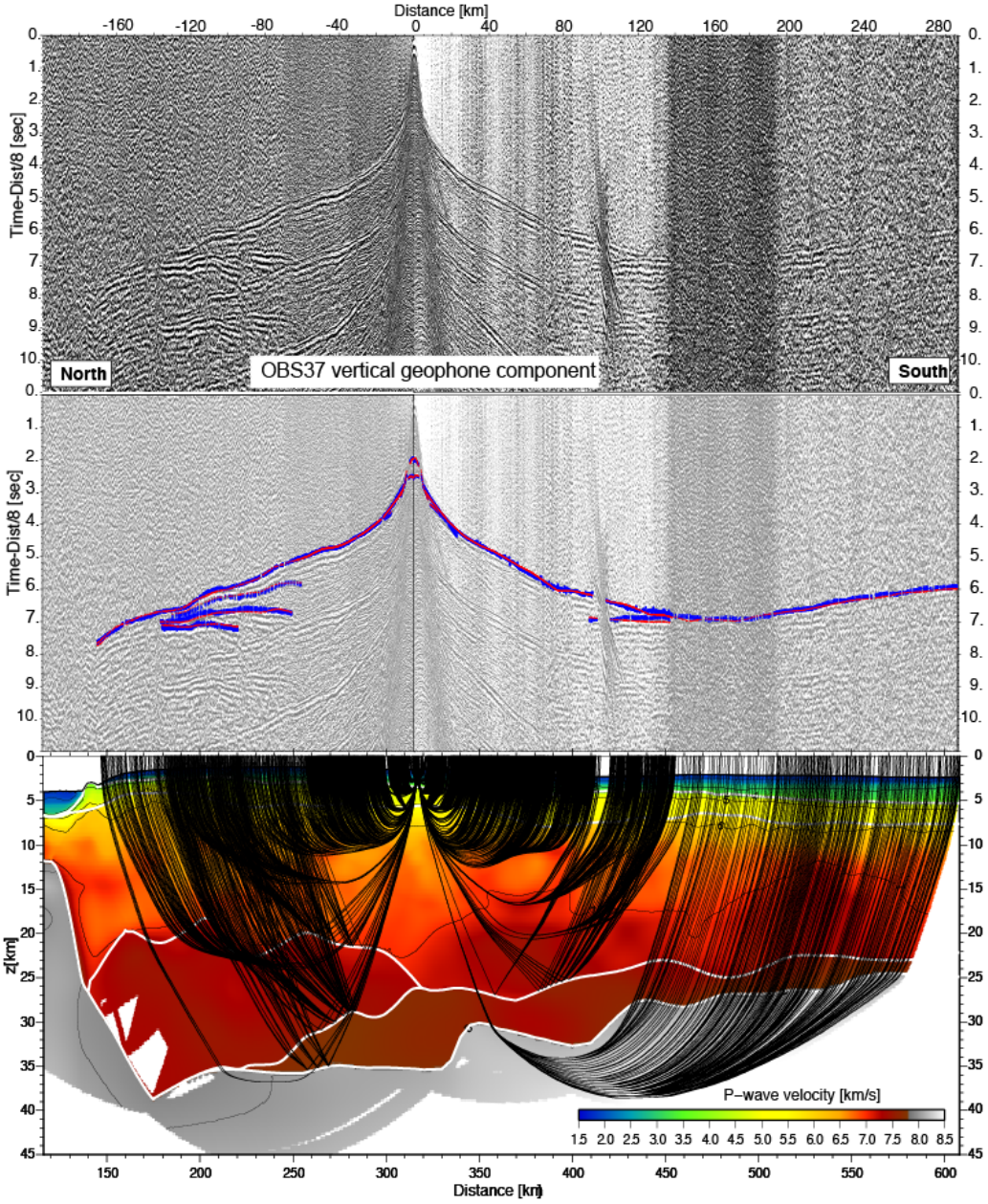

Fig. DR5: Data example for an OBS station of profile 3.

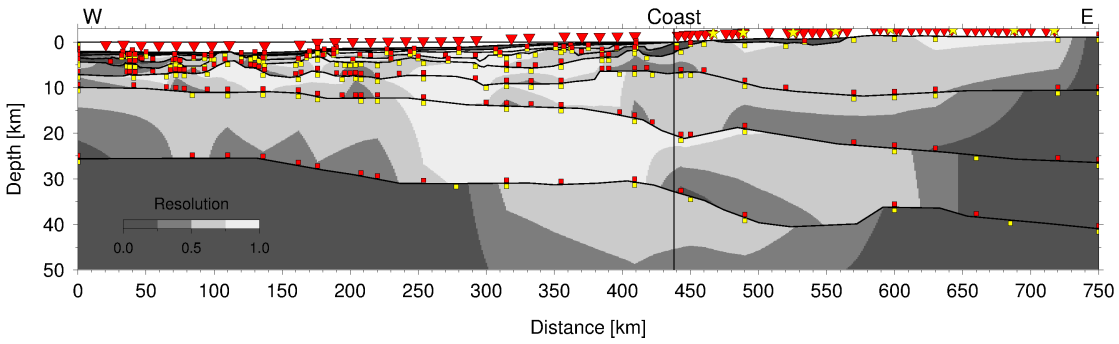

Fig. DR6: Resolution for profile 100. The model is well resolved in the area of the high velocity body in the lower crust (km 250 to 420), although the resolution drops at both ends of the HVLCB.

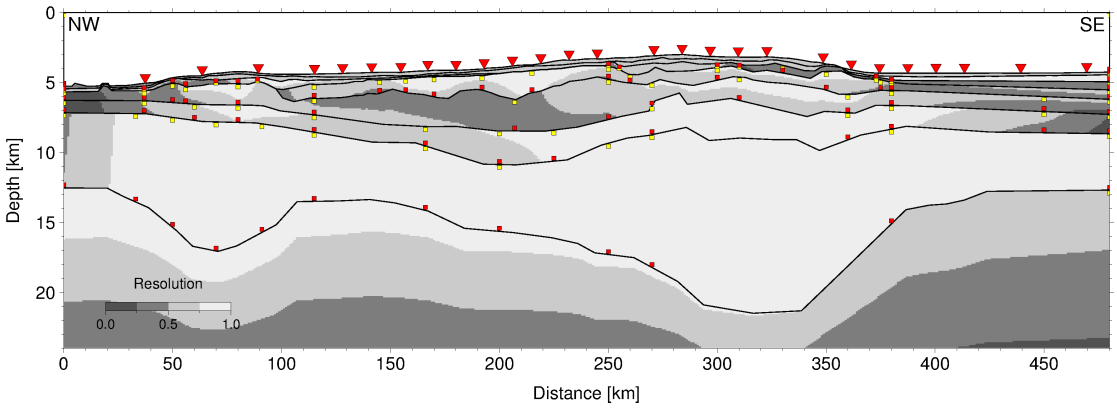

Fig. DR7: Resolution for profile 150. The model is well resolved in the lower crust. The lower resolution north of the ridge (LVZ) is due to a velocity inversion, which does not produce refracted waves and is therefore only constrained by reflections.

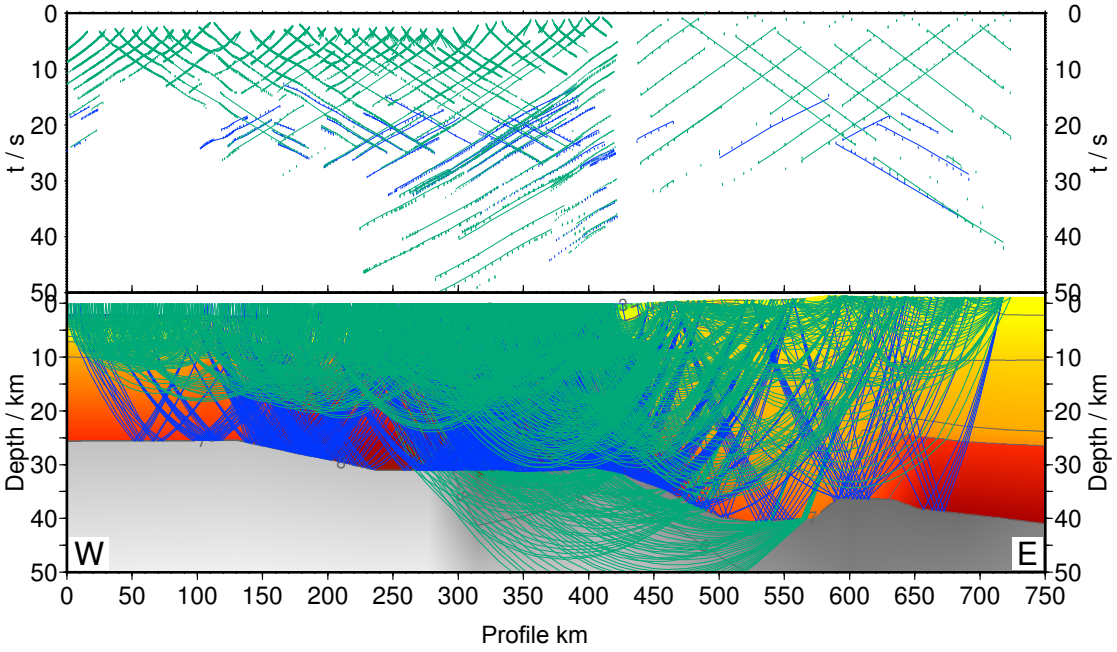

Fig. DR8: Ray tracing results (top) and ray coverage (bottom) for all stations of profile 100.

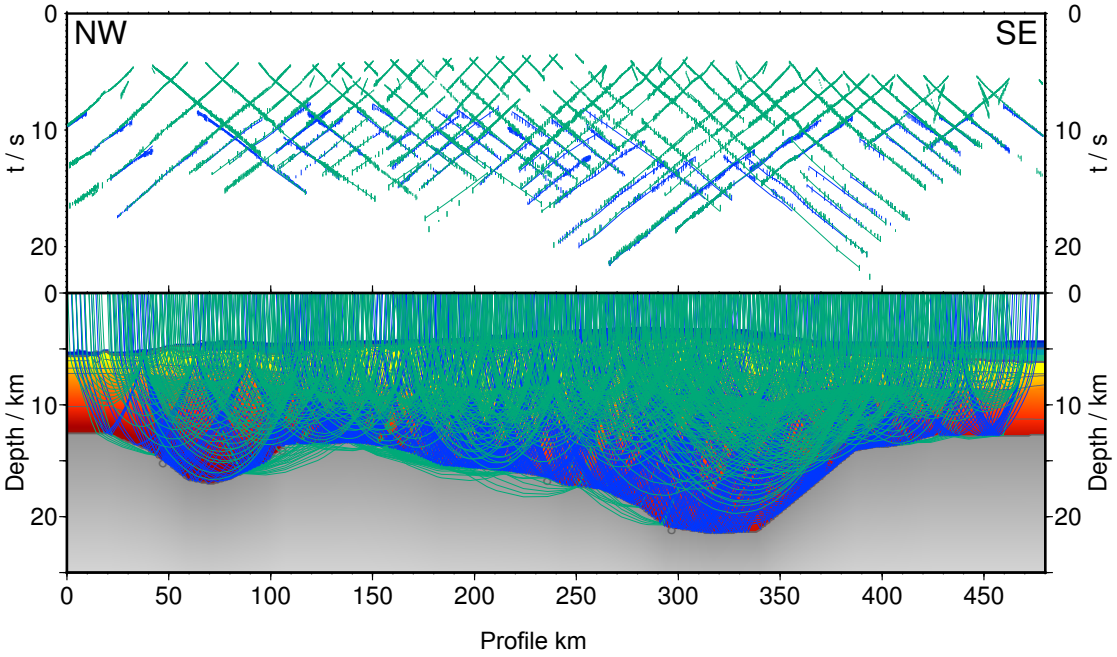

Fig. DR9: Ray tracing results (top) and ray coverage (bottom) for all stations of profile 150.

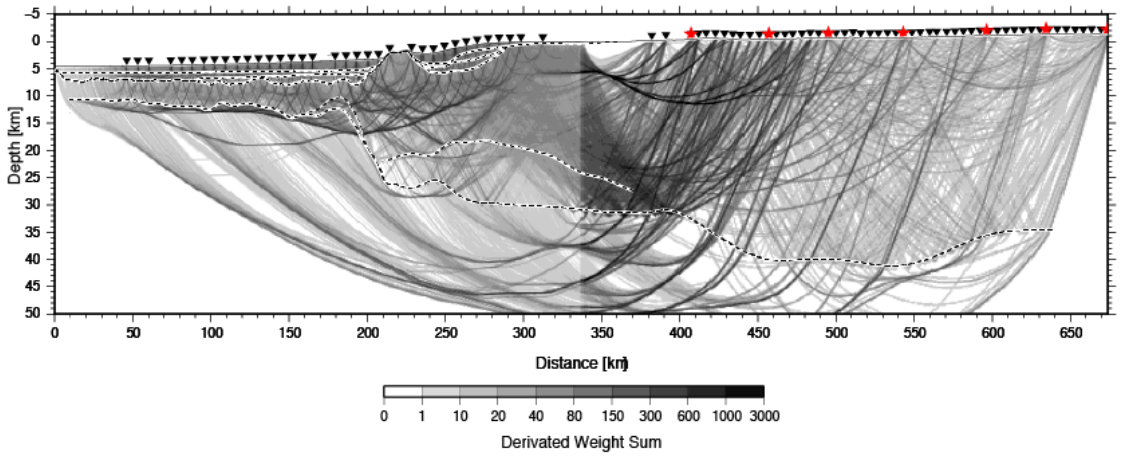

Fig. DR10: Derivative weight sum (DWS) of profile 2.

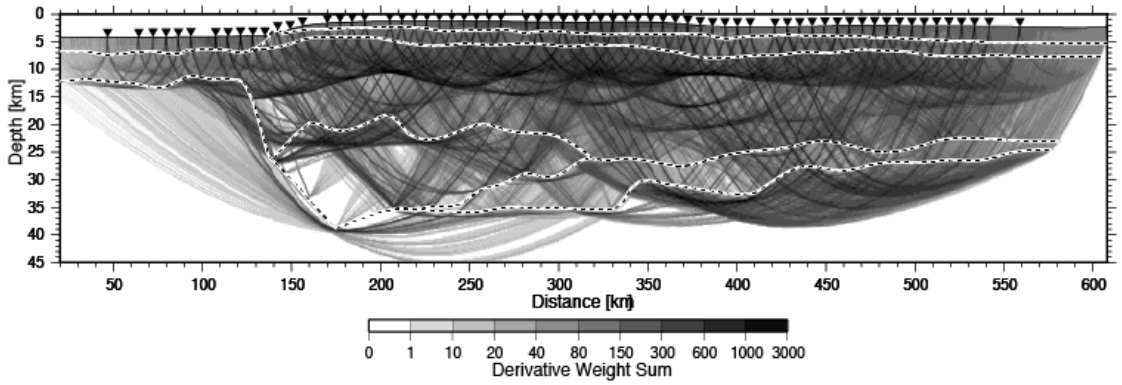

Fig. DR11: Derivative weight sum (DWS) of profile 3 (c.f. caption Fig. DR10).

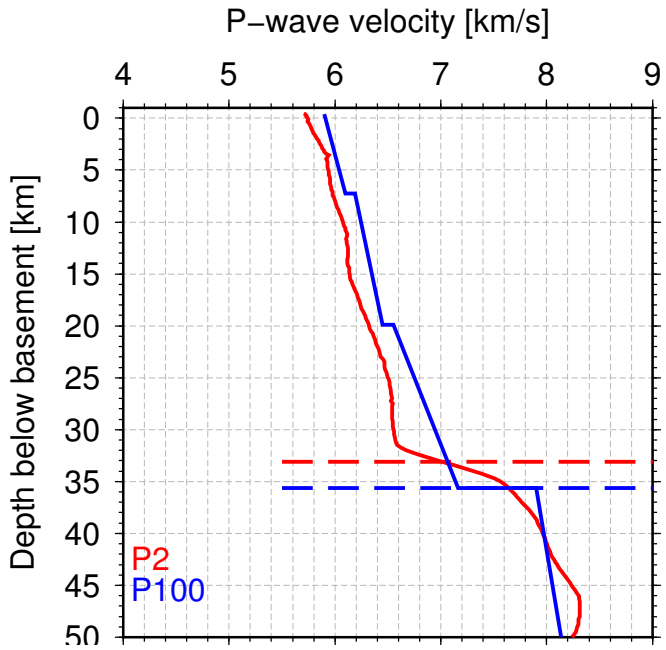

Fig. DR12: Comparison of the velocity depth relation of profiles 100 and 2 at the intersection on land (km 466 at P100 and km 410 at P2). The dashed lines indicate the Moho depth.